Int. J. Appl. Math. Comput. Sci., 2026, Vol. 36, No. 1, 23–35
DOI: 10.61822/amcs-2026-0003

ON THE GAIN SYNTHESIS OF DYNAMIC AND INTEGRAL SLIDING MODE CONTROLLERS FOR QUAD ROTORCRAFT TRAJECTORY TRACKING

DANIEL BENÍTEZ [a], JOVANI ORTEGA [a], PATRICIO ORDAZ [a,*], EDUARDO S. ESPINOZA [b,c]

[a] Academic Department of Computing and Electronics
Autonomous University of the State of Hidalgo
Carr. Pachuca–Tulancingo Km. 4.5, Colonia Carboneras, Mineral de la Reforma, Hidalgo, 42184, Mexico
e-mail: {be409784,jovani_ortega,jesus_ordaz}@uaeh.edu.mx

[b] Directorate of Support for the Consolidation of the Scientific and Humanistic Community
Secretariat of Science, Humanities, Technology, and Innovation
Av. Insurgentes Sur 1582, Col. Crédito Constructor, Alc. Benito Juárez, Mexico City, 03940, Mexico
e-mail: eespinoza@secihti.mx

[c] Department of Research and Multidisciplinary Studies
Center For Research and Advanced Studies of the National Polytechnic Institute
Av. Instituto Politécnico Nacional 2508, Col. San Pedro Zacatenco, Alc. Gustavo A. Madero, Mexico City, 07360, Mexico
e-mail: eduardo.espinoza@cinvestav.mx

This study explores the development of two control strategies based on the sliding mode approach for quad rotorcraft trajectory tracking. A dynamic and an integral-type controller are designed to ensure that the sliding surface reaches zero within a finite time, resulting in a PD-like structure. Since this structure aids in determining the gains of robust PD controllers, it is utilized for comparative analysis. To account for uncertain dynamics and external disturbances, this work proposes an offline linear matrix inequality (LMI) algorithm that guarantees ultimate uniform stability for both sliding mode controllers. The primary advantage of the proposed LMI-based strategy is its ability to simplify the implementation of a sliding mode controller in complex systems, overcoming challenges associated with their intricate tuning process. Since the proposed algorithm applies to all three controllers, it facilitates the identification of the most effective one based on the system's dynamic response. A comparative analysis based on error criteria is performed through numerical simulations to validate the effectiveness of the proposed strategies. In addition, a second comparative analysis is conducted between two widely used robust control strategies from the literature and the proposed ISMC. Finally, the effectiveness of the designed algorithm is evaluated using a complex reference trajectory featuring high maneuverability and high-speed flight.

Keywords: gain tuning, sliding mode control, linear matrix inequalities, trajectory tracking, robust control.

1. Introduction

Unmanned aerial vehicles (UAVs) have been constantly evolving and changing in size, shape, capabilities, and applications. Because UAVs can be used in a variety of applications, they can encounter adverse conditions such as strong wind gusts. A disturbance like that represents the type with the highest rate of occurrence when flying outdoors (Ahmad *et al.*, 2022). Wind gusts significantly affect vehicle behavior during flight, which makes it essential to develop robust control techniques to mitigate their effects. To deal with this type of disturbance, different control strategies have been developed to provide robustness against it. Eltayeb *et al.* (2020) designed an improved adaptive sliding mode controller that changes the value of the controller gain according to the uncertainties of the parameters. Raiesdana (2020) used terminal sliding mode control with the implementation of a neuronal network learning process to synthesize the control parameters. Rehman *et al.* (2021) employed sliding mode control with a

*Corresponding author

parabolic sliding surface to converge to the sliding surface faster than the conventional method. Da Silva and Moreira (2022) applied sliding mode control and implemented a Gaussian process regression for uncertainty estimation and compensation.

Alternatively, a robust approach based on finite-time Lyapunov stability was proposed by García *et al*. (2019), where the strategy was evaluated using backstepping for the position and attitude control of a UAV. Additionally, controllers based on linear quadratic regulators (Ordaz *et al*., 2018), adaptive algorithms (Mofid *et al*., 2021), and PID controllers combined with continuous sliding mode controllers (Ríos *et al*., 2019) serve as precedents for strategies aimed at robust trajectory tracking and mitigating external disturbances and uncertainties.

Sliding mode control strategies have been widely used in UAV applications due to their key advantage: the dynamic behavior of the system can be shaped by appropriately selecting switching functions, rendering the closed-loop response completely insensitive to certain uncertainties, nonlinear dynamics, and external disturbances (Eker, 2006). However, a major drawback is the well-known chattering phenomenon, which occurs due to the use of the sign function in the control law designed to stabilize the sliding surface.

To address this undesirable phenomenon while minimizing the effects of external disturbances, researchers have proposed various solutions, including integral sliding mode controllers (ISMCs) and dynamic sliding mode controllers (DSMCs). These two controllers incorporate diverse types of sliding surfaces such as those resembling PID control (Ullah *et al*., 2020) or solutions of differential equations based on system dynamics (Roux *et al*., 2023) to enhance system robustness against external disturbances. Although ISMCs have demonstrated better performance in handling disturbances compared to DSMCs, the control signal they generate leads to higher frequency chattering than that of DSMCs does. In contrast, because DSMCs are dynamic, their integration produces a control signal that effectively reduces chattering.

On the other hand, several authors have focused on analyzing different types of sliding mode controllers by comparing strategies such as singular terminal sliding modes, continuous non-singular sliding modes, and continuous twisting control to handle external disturbances like wind gusts effectively. In this context, Falcón *et al*. (2019) determined that trajectory tracking applications under wind gusts achieve better performance when using continuous twisting control. Similarly, several studies have been conducted to compare the performance of control laws based on first-order sliding modes, second-order sliding modes, fast terminal sliding modes, and integral sliding modes. In this comparison, the ISMC exhibited the best performance in terms of robustness and fast convergence (Din *et al*., 2018). Furthermore, comparative studies have been conducted on sliding mode control strategies using different sliding surfaces. For instance, Khan and Nasreen (2021) compared a linear sliding surface with an integral sliding one. The results showed that the system state error converged faster with the linear sliding surface than with the integral one.

However, despite the successful implementation of ISMCs by various authors (e.g., Yongwei and Shunchao, 2024), controller gains are typically determined using heuristic methods or the Hurwitz criterion. Alternatively, Lei *et al*. (2024) proposed employing LMIs within an ISMC framework for the nominal control of an uncertain impulsive stochastic system, ensuring that the controlled system remains uniformly almost exponentially stable. Similarly, authors such as Herrera *et al*. (2020) previously implemented DSMCs with sliding surfaces based on PD or PID controllers, where gains were also derived through heuristic approaches. Despite the development of sliding mode strategies by various authors (e.g., Ahmad *et al*., 2022) to handle uncertainties and external disturbances, most of these approaches do not account for the disturbances encountered in real-time applications. Instead, disturbances are typically modeled as constant parameters or simple time-varying functions.

In this research work, a dynamic and an integral type controller are designed to guarantee that the sliding surface of the sliding mode controllers reaches zero within a finite time. To account for uncertain dynamics and external disturbances for quad rotorcraft trajectory tracking, this work proposes an offline LMI-based algorithm to synthesize the controller gains guaranteeing ultimate uniform stability for both sliding mode controllers. Since the resulting PD-like structure aids in determining the gains of robust PD controllers, it is utilized for comparative analysis.

The proposed LMI-based strategy simplifies the implementation of sliding mode controllers in complex systems, overcoming challenges associated with their intricate tuning process.

Furthermore, since the proposed algorithm applies to all three controllers, it facilitates the identification of the most effective controller based on the dynamic response of the system.

The main contributions of this research work are summarized as follows.

- The performance of each proposed controller is compared in stabilizing the altitude, longitudinal, lateral, and directional subsystems of a quad rotorcraft, all subject to wind gusts modeled by the Dryden wind turbulence model.

- The sliding surface for the ISMC is designed to enhance disturbance rejection and uncertainties in

the dynamics coupled to the control, whereas the nominal controller gains are obtained by using an LMI approach. Unlike Lei *et al*. (2024), who applied ISMC and LMI theory to solve control gains in uncertain impulsive stochastic systems, this study considers a class of nonlinear underactuated system as its application.

The proposed PD structure on the sliding surface of the DSMC reduces the effects of disturbances and mitigates chattering without compromising robustness.

A comparative analysis based on error criteria is performed through numerical simulations to validate the effectiveness of the proposed strategies. In addition, due to the nature of the variable structure, the energy consumption of the three strategies is determined, allowing us to analyze the adverse effects of the chattering phenomenon. A second comparative analysis is conducted between two widely used robust control strategies from the literature and the proposed ISMC. In addition, the effectiveness of the designed algorithm is evaluated using a complex reference trajectory featuring high maneuverability and high-speed flight.

The remainder of the paper is structured as follows. The UAV model and problem statement description are presented in Section 2. The design of robust controllers for a specific class of disturbances is discussed in Section 3. An illustrative scenario for regulating the quad rotorcraft, focusing on trajectory tracking, is presented in Section 4. Finally, Section 5 contains concluding remarks.

2. UAV model

Quadrotors can adjust their orientation and position using their four control inputs. The drone can control its roll, pitch, yaw, and altitude dynamics by changing the speed of its four rotors. When the orientation of the vehicle changes, it results in a translational displacement. Translational movement is described by the location of its center of mass in a three-dimensional inertial reference frame fixed to the Earth, whereas its orientation is described in a reference frame attached to the vehicle. Figure 1 shows the configuration and characteristics of the UAV used in this study.

The translational dynamic equations are described as follows (García *et al*., 2013):

$$\begin{aligned} M\ddot{p}_x &= u_z(\sin\phi\sin\psi + \cos\phi\cos\psi\sin\theta) + \Delta_x,\\ M\ddot{p}_y &= u_z(\cos\phi\sin\theta\sin\psi - \cos\psi\sin\phi) + \Delta_y,\\ M\ddot{p}_z &= u_z\cos\theta\cos\phi - Mg + \Delta_z, \end{aligned} \tag{1}$$

where $\varrho = (p_x, p_y, p_z)^\intercal$ denotes the position of the vehicle's center of mass relative to the inertial reference frame I; Δ_x, Δ_y and Δ_z denote the external disturbance in p_x, p_y and p_z, respectively; u_z is the control input in the z direction from the force of each rotor; M is the mass

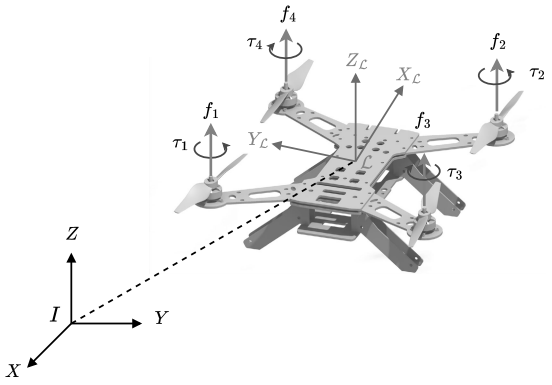

Fig. 1. Multirotor vehicle.

of the vehicle; g is the gravity constant; ϕ (roll), θ (pitch) and ψ (yaw) represent the orientation of the vehicle. On the other hand, the rotational dynamics are given as

$$\mathbf{J}\ddot{\eta} = \mathbf{C}(\eta,\dot{\eta})\dot{\eta} + \tau, \tag{2}$$

where $\eta = (\phi,\theta,\psi)^\intercal \in \mathbb{R}^3$ holds the Euler angles of the body frame $\mathcal{L}$; $\mathbf{J}$ is the inertia matrix for the kinetic energy; $\mathbf{C}(\eta,\dot{\eta})^\intercal$ represents the Coriolis terms containing the gyroscopic and centrifugal effects associated with η; $\tau = (u_\phi, u_\theta, u_\psi)^T$ stands for the moments of roll, pitch and yaw angles.

Assumption 1. The roll and pitch angles are restricted to $\theta \in (-\pi/2,\ \pi/2)$ and $\phi \in (-\pi/2,\ \pi/2)$.

Assumption 2. Given that the UAV's maximum velocity is limited by the maximum available thrust, there is a positive constant $\lambda_{ci\eta 0}$ and $\lambda_{ci\eta 1}$ such that $\|\mathbf{C}_i(\eta,\dot{\eta})\|_\infty \le \lambda_{ci\eta 0} \parallel \eta \parallel + \lambda_{ci\eta 1} \parallel \dot{\eta} \parallel_\infty$.

In this way, Eqn. (2) can be expressed as

$$\ddot{\eta} = \mathbf{J}^{-1}\mathbf{C}(\eta,\dot{\eta})\dot{\eta} + \mathbf{J}^{-1}\tau \tag{3}$$

and $\mathbf{J}^{-1} = diag(\gamma_\phi,\gamma_\theta,\gamma_\psi)$, where $\gamma_\phi = 1/J_\phi$, $\gamma_\theta = 1/J_\theta$, and $\gamma_\psi = 1/J_\psi$. Defining $e_\eta = \eta - r_\eta$ and r_η as the desired angle trajectory, the corresponding error dynamics yield

$$\ddot{e}_\eta = \ddot{\eta} - \ddot{r}_\eta = \mathbf{J}^{-1}\tau + \zeta_\eta, \tag{4}$$

where

$$\zeta_\eta = \mathbf{J}^{-1}\mathbf{C}(\eta,\dot{\eta})\dot{\eta} - \ddot{r}_\eta \tag{5}$$

and external disturbances given by ζ_η are bounded. Furthermore, it is assumed that the desired reference is a smooth function. Consequently, equations for the dynamics of the orientation error are derived as shown by Liu *et al*. (2014):

$$\begin{aligned} \ddot{e}_\phi &= \gamma_\phi u_\phi + \zeta_\phi,\\ \ddot{e}_\theta &= \gamma_\theta u_\theta + \zeta_\theta,\\ \ddot{e}_\psi &= \gamma_\psi u_\psi + \zeta_\psi. \end{aligned} \tag{6}$$

2.1. Altitude dynamics. For the reduced system of translation in p_z, the dynamics of the height error are given by

$$\ddot{e}_z = \ddot{p}_z - \ddot{r}_z = \frac{u_z}{M}\cos\theta\cos\phi - g + \frac{\Delta_z}{M} - \ddot{r}_z, \quad (7)$$

where r_z is the desired reference value at p_z. Pre-control of the linearizing compensation type is defined as $u_z = M(g+u_{zz})/(\cos\theta\cos\phi)$, where the control input $u_{zz} = -k_{z1}e_z - k_{z2}\dot{e}_z$ is introduced to stabilize the altitude dynamic. After substituting and reducing terms, the following error equation is obtained:

$$\ddot{e}_z = -k_{z1}e_z - k_{z2}\dot{e}_z + \zeta_z, \quad (8)$$

where

$$\zeta_z = -\ddot{r}_z + \Delta_z. \quad (9)$$

Finally, the error in altitude dynamics is defined as $x_z = [e_{z1}, e_{z2}]^\intercal$.

2.2. Heading dynamics. Equation (6) considers the dynamics of the error from ψ to define the control input u_ψ as follows:

$$u_\psi = \frac{-k_{\psi1}e_\psi - k_{\psi2}\dot{e}_\psi}{\gamma_\psi}. \quad (10)$$

This is related to the desired dynamics for ψ by $\ddot{e}_\psi = -k_{\psi1}e_\psi - k_{\psi2}\dot{e}_\psi + \zeta_\psi$, with $k_{\psi1}, k_{\psi2}$ being the control gains. In this case, the error vector associated with the ψ dynamics is defined as $x_\psi = [e_{\psi1}, e_{\psi2}]^\intercal$.

2.3. Longitudinal dynamics. Consider p_x dynamics after replacing u_z:

$$\ddot{p}_x = \left(\tan\theta\cos\psi + \tan\phi\,\frac{\sin\psi}{\cos\theta}\right)(g+u_{zz}) + \Delta_x. \quad (11)$$

The error function is defined as $\ddot{e}_{p_x} = \ddot{p}_x - \ddot{r}_x$ and the desired dynamic as

$$\ddot{e}_{p_x} = -k_{x1}e_{p_x} - k_{x2}\dot{e}_{p_x}, \quad (12)$$

where k_{x1}, k_{x2} are control gains.

Then, substituting and isolating the term $\tan\theta$ yields

$$\tan\theta = \left(\frac{-k_{x1}e_{p_x} - k_{x2}\dot{e}_{p_x} + \ddot{r}_x}{g+u_{zz}} - \kappa\right)\frac{1}{\cos\psi} + \zeta_x,$$
$$\kappa = \tan\phi\,\frac{\sin\psi}{\cos\theta}. \quad (13)$$

Note that the subsystem $x-\theta$ in UAV dynamics p_x can be controlled indirectly by manipulating θ. In this way, $\tan\theta$ functions as a virtual control input that ensures the tracking error of θ converges to zero relative to the reference signal (r_θ). Hence, if θ is satisfied, the dynamic in x is controlled. Thus, it is proposed that the error in θ is $e_\theta = \theta - r_\theta$. Notice that r_θ is described as

$$r_\theta = \arctan\left\{\left(\frac{-k_{x1}e_{p_x} - k_{x2}\dot{e}_{p_x} + \ddot{r}_x}{g+u_{zz}} - \kappa\right)\frac{1}{\cos\psi} + \zeta_x\right\}. \quad (14)$$

From the referent error function θ in (1), the control input is defined as $\ddot{e}_\theta = -k_{\theta1}e_\theta - k_{\theta2}\dot{e}_\theta + \zeta_\theta$, where

$$u_\theta = \frac{(-k_{\theta1}e_\theta - k_{\theta2}\dot{e}_\theta + \ddot{r}_\theta)}{\gamma_\theta}. \quad (15)$$

2.4. Lateral dynamics. Consider p_y dynamics after replacing u_z:

$$\ddot{p}_y = \left(\tan\theta\,\sin\psi - \tan\phi\,\frac{\cos\psi}{\cos\theta}\right)(g+u_{zz}) + \Delta_y. \quad (16)$$

On the other hand, the error function is defined by $\ddot{e}_{p_y} = \ddot{p}_y - \ddot{r}_y$ and the desired dynamic as

$$\ddot{e}_{p_y} = -k_{y1}e_{p_y} - k_{y2}\dot{e}_{p_y}, \quad (17)$$

with k_{y1}, k_{y2} as control gains. So, substituting into (16), we have

$$\tan\phi = \left(\frac{k_{y1}e_{p_y} + k_{y2}\dot{e}_{p_y} - \ddot{r}_{p_y}}{g+u_z} + \iota\right)\frac{\cos\theta}{\cos\psi} + \zeta_y,$$
$$\iota = \tan\theta\sin\psi. \quad (18)$$

Notably, p_y can be indirectly controlled by adjusting ϕ. This allows for virtual control over p_y through the term $\tan\ \phi$. Subsequently, the ϕ error is proposed as $e_\phi = \phi - r_\phi$, and r_ϕ is described as

$$r_\phi = \arctan\left\{\left(\frac{k_{y1}e_{p_y} + k_{y2}\dot{e}_{p_y} - \ddot{r}_y}{g+u_z} + \iota\right)\frac{\cos\theta}{\cos\psi} + \zeta_y\right\}. \quad (19)$$

Finally, the error dynamic of ϕ is expressed as $\ddot{e}_\phi = -k_{\phi1}e_\phi - k_{\phi2}\dot{e}_\phi + \zeta_\phi$, and the control input is given as follows:

$$u_\phi = \frac{(-k_{\phi1}e_\phi - k_{\phi2}\dot{e}_\phi + \ddot{r}_\phi)}{\gamma_\phi}. \quad (20)$$

Without loss of generality, after the previous dynamic reduction, each UAV subsystem can be represented as a quasi-linear system as follows:

$$\dot{x}_i = \mathbf{A}x_i + B_iu_i + \zeta_i, \quad (21)$$

$$\mathbf{A} = \begin{bmatrix} 0 & 1 \\ 0 & 0 \end{bmatrix}, \quad B_i = \begin{bmatrix} 0 \\ q_i \end{bmatrix}, \ i = x, y, z, \phi, \theta, \psi. \tag{22}$$

For $i = x, y, z$, the coefficient q_i takes the value $q_i = 1$, and for $i = \phi, \theta, \psi$, $q_i = \gamma_i$.

Now, let us examine Eqn. (21), which represents the dynamics of a quadrotor aircraft affected by wind gusts and unmodeled dynamics as described in the previous differential equation. Here, the matrix $\mathbf{A} \in \mathbb{R}^{2\times 2}$ is the state matrix, $B_i \in \mathbb{R}^2$ is the vector associated with the control input, and the vector $\zeta(t, x)$ contains the external disturbances and/or uncertain dynamics. Thus, the problem involves proposing an input u that allows the vehicle to follow a trajectory while also rejecting disturbances such as wind. The following section studies the design of robust controllers using the concept of uniformly ultimately bounded stability (UUB).

Remark 1. The translational positions of the vehicle are related to the attitude control response, and therefore the desired orientation is different for each of the controllers to be designed.

Definition 1. (*UUB stability* (*Poznyak* et al., *2014*)) The solution of (21) is UUB stable with a limit or final bound b if there is a positive constant $c > 0$ independent of $t_0 \geq 0$, such that for an $a \in (0, c)$ there is $T = T(a, b) > 0$ such that

$$\| x(t_0) \| \leq a \Rightarrow \| x(t) \| \leq b, \quad \forall\, t \geq t_0 + T. \tag{23}$$

3. Control strategies design

3.1. Dynamic sliding mode control. The system (21) can be rewritten as in the work of Ullah *et al*. (2020):

$$\begin{aligned} \dot{x}_{i1} &= \mathbf{A}_{11}x_{i1} + \mathbf{A}_{12}x_{i2} + \zeta_{i1}(t), \\ \dot{x}_{i2} &= \mathbf{A}_{21}x_{i1} + \mathbf{A}_{22}x_{i2} + B_{i2}u_h + \zeta_{i2}(t), \end{aligned} \tag{24}$$

where $h = zz,\ \psi,\ \theta,\ \phi$; $\mathbf{A}_{11}$, $\mathbf{A}_{12}$, $\mathbf{A}_{21}$, $\mathbf{A}_{22}$, $B_{i2} \in \mathbb{R}$, are associated with the state vector $x = \begin{bmatrix} x_{i1}^\intercal & x_{i2}^\intercal \end{bmatrix}^\intercal$, with x_{i1} y $x_{i2} \in \mathbb{R}$. The terms ζ_{i1} and ζ_{i2} satisfy the following restrictions:

$$\|\zeta_{i1}(t)\|^2 \leq c_1,\ \|\zeta_{i2}(t)\|^2 \leq c_2,\ 0 < (c_1, c_2) < \infty. \tag{25}$$

Consider a storage function given as

$$V_i(\sigma_i) = \frac{1}{2}\sigma_i^\intercal \sigma_i, \tag{26}$$

with the sliding manifold proposed as

$$\sigma_i = k_i x_z + B_{i2}u_h,\ \ \sigma_i \in \mathbb{R},\ k_i = \begin{bmatrix} k_{i1} & k_{i2} \end{bmatrix}. \tag{27}$$

Knowing k_i, it is assumed that $|k_i\zeta_i(x, t)| \leq \delta_i$.

Proposition 1. *Consider the representation of the system given by* (24) *and the sliding variable* (27)*. If the control signal u_h exhibits the following dynamics:*

$$\begin{aligned} \dot{u}_h = -B_{i2}^{-1}\{&k_{i1}\left(\mathbf{A}_{11}x_{i1} + \mathbf{A}_{12}x_{i2}\right) \\ &+ k_{i2}\left(\mathbf{A}_{21}x_{i1} + \mathbf{A}_{22}x_{i2} + B_{i2}u_h\right) \\ &+ \rho_i \text{sign}(\sigma_i(t))\}, \\ u_h(0) = u_{i0}, \quad 0 < \rho_i \in \mathbb{R}, \quad &\delta_1 < \lambda_{\min}(\rho) := \delta_i, \end{aligned} \tag{28}$$

then, after time $t_r \leq \frac{\sqrt{2}}{\gamma}V^{\frac{1}{2}}(\sigma_i(t_0)) + t_0$, the sliding manifold (27) *reaches the sliding motion $\sigma_i(t) = 0$.*

The proof of Proposition 1 is as follows.

Proof. Let us define the time variation of the storage function (26) as

$$\dot{V}_i(\sigma) = \sigma_i^\intercal(t)\left(k_{i1}\dot{x}_{i1} + k_{i2}\dot{x}_{i2} + B_{i2}\dot{u}_h\right). \tag{29}$$

By considering the dynamic control law given by (28), the following statement is derived:

$$\dot{V}_i(\sigma) = \sigma_i^\intercal(t)\left(k_{i1}\zeta_{i1}(t) + k_{i2}\zeta_{i2}(t) - \rho_i \text{sign}(\sigma_i(t))\right). \tag{30}$$

Normalizing the previous equation and using the constraints given in (25), the following inequality yields

$$\begin{aligned} \dot{V}_i(\sigma) &\leq \delta_1|\sigma_i(t)| - \sigma_i^\intercal(t)\rho_i \text{sign}(\sigma_i(t)) \\ &\leq |\sigma_i(t)||k_{i1}c_1 + k_{i2}c_2| - \lambda_{\min}(\rho)|\sigma_i(t)|. \end{aligned} \tag{31}$$

By considering that $0 < \lambda_{\min}(\rho) - \delta_i = \gamma$, the next inequality is obtained:

$$\dot{V}_i(\sigma) \leq -\gamma|\sigma_i(t)| = -\sqrt{2}\gamma V^{\frac{1}{2}}(\sigma_i), \tag{32}$$

which indicates that σ_i converges after time $t \leq t_r$, and Proposition 1 is proved. ∎

Assuming that Proposition 1 is satisfied, the sliding motion is induced after time $t \leq t_r$, so, $\sigma = 0$ and $\dot{\sigma} = 0$. This implies $\dot{u}_h = (B_{i2}K_i x_i)^{-1}$, and the closed-loop system (24) yields

$$\begin{aligned} \dot{x}_i &= (\mathbf{A} - k_i)x_i + \Delta_i(x_i, t), \\ \Delta_i(x_i, t) &= \begin{bmatrix} k_{i1}^\intercal\left(\mathbf{L}\right)^{-1}\rho_i & -k_{i1}^\intercal\left(\mathbf{L}\right)^{-1}k_{i2} \\ 0 & 1 \end{bmatrix}\begin{bmatrix} \text{sign}(\sigma_i) \\ \zeta_{i2}(x_i, t) \end{bmatrix}, \\ x_i(t_r) &= x_{it_r},\ t_r \leq t \in \mathbb{R}^+, \end{aligned} \tag{33}$$

where $\mathbf{L} = k_{i1}k_{i1}^\intercal$. The procedure for deriving Eqn. (33) is detailed by Ordaz *et al*. (2019). The problem statement is to get a gain K_i to ensure the stability of (33) robustly, specifically in the context of UUB stability in this study. Furthermore, if k_{i1} is large in magnitude, then the term $k_{i1}^\intercal\left(k_{i1}k_{i1}^\intercal\right)^{-1}$ is small; therefore, uncoupled uncertainties

are rejected. The next step in designing the control strategy is to obtain the necessary conditions to ensure the UUB stability of the system (33). To achieve this, let us consider Proposition 2, which is used to deduce the gains of the PD robust controller by solving a convex optimization problem.

Proposition 2. *If there exists a set of solutions ($0 < \alpha$, $0 < \varepsilon$, $0 < \boldsymbol{P} \in \mathbb{R}^{2\times 2}$ and $K_i \in \mathbb{R}^{1\times 2}$) such that the matrix inequality*

$$\mathbf{W}_i = \begin{bmatrix} \mathbf{P}(\mathbf{A} - B_i k_i) + (\mathbf{A} - k_i B_i)^{\mathsf{T}}\mathbf{P} + \alpha\mathbf{P} & \mathbf{P} \\ \mathbf{P} & -\varepsilon I \end{bmatrix} < 0 \tag{34}$$

holds, then the system (33) *arrives at the invariant set*

$$\Omega = \left\{ x_i(t) \in \mathbb{R}^n \,\middle|\, \|x_i\|^2 \le \frac{\varepsilon\delta}{\lambda_{\min}(\mathbf{P})\alpha} \right\} \tag{35}$$

in finite time,

$$b = \frac{\varepsilon\delta + \alpha\gamma}{\alpha}, \quad T = \frac{1}{\alpha}\ln\left\{\frac{\alpha V(t_0) - \varepsilon\delta}{\varepsilon\delta\gamma}\right\} + t_0, \tag{36}$$

for a sufficiently small positive scalar γ. This means that the system is stable in the UUB sense.

Proof. The gain matrix k_z is determined through an analysis of the following energy function:

$$V_1(x_i) = x_i^{\mathsf{T}}\mathbf{P}x_i, \tag{37}$$

where $\mathbf{P} \in \mathbb{R}^{2\times 2}$ is a positive definite matrix. The time derivative of the energy function along the trajectories of the system is given as

$$\begin{aligned}\dot{V}_1(x_i) = {} & x_i^{\mathsf{T}}\mathbf{P}\{\mathbf{A}x_i - B_i k_i x_i + \zeta_i\} \\ & + \{x_i^{\mathsf{T}}\mathbf{A}^{\mathsf{T}} - x_i^{\mathsf{T}}k_i^{\mathsf{T}}B_i^{\mathsf{T}} + \zeta_i^{\mathsf{T}}\}\mathbf{P}x_i,\end{aligned} \tag{38}$$

with $u_h = -k_i x_i$. Notice that (38) is equivalent to

$$\dot{V}_1(x_i) = \begin{bmatrix} x_i^{\mathsf{T}} \\ \zeta_i^{\mathsf{T}} \end{bmatrix} \begin{bmatrix} \mathbf{P}\mathbf{A} - \mathbf{Q} + \mathbf{A}^{\mathsf{T}}\mathbf{P} - \mathbf{Q}^{\mathsf{T}} & \mathbf{P} \\ \mathbf{P} & 0 \end{bmatrix} \begin{bmatrix} x_i \\ \zeta_i \end{bmatrix}, \tag{39}$$

where $\boldsymbol{Q} = \mathbf{P}B_i K_i$. By adding and subtracting the terms $\alpha V_1(x_i)$, $\varepsilon\|\zeta_i\|^2$, for the positive scalars α and ε, the following expression is obtained:

$$\begin{aligned}\dot{V}_1(x_i) = {} & \begin{bmatrix} x_i \\ \zeta_i \end{bmatrix}^{\mathsf{T}} \begin{bmatrix} \mathbf{P}\mathbf{A} - \mathbf{Q} + \mathbf{A}^{\mathsf{T}}\mathbf{P} - \mathbf{Q}^{\mathsf{T}} + \alpha\mathbf{P} & \mathbf{P} \\ \mathbf{P} & -\varepsilon\boldsymbol{I} \end{bmatrix} \\ & \times \begin{bmatrix} x_i \\ \zeta_i \end{bmatrix} - \alpha V_1(x_i) + \varepsilon\|\zeta_i\|^2,\end{aligned} \tag{40}$$

which is equivalent to

$$\dot{V}_1(x_i) = \begin{bmatrix} x_i \\ \zeta_i \end{bmatrix}^{\mathsf{T}} \mathbf{W_i} \begin{bmatrix} x_i \\ \zeta_i \end{bmatrix} - \alpha V_1(x_i) + \varepsilon\|\zeta_i\|^2 \ , \tag{41}$$

where $\boldsymbol{W}_i$ is given by (34). Now, assuming that $\|\zeta_i\|^2 \le \delta$,

$$\dot{V}_1(x_i) \le \begin{bmatrix} x_i \\ \zeta_i \end{bmatrix}^{\mathsf{T}} \mathbf{W}_i \begin{bmatrix} x_i \\ \zeta_i \end{bmatrix} - \alpha V_1(x_i) + \varepsilon\delta, \tag{42}$$

and, if $\mathbf{W}_i = \mathbf{W}_i^{\mathsf{T}} < 0$, then

$$\begin{aligned}\dot{V}_1(x_i) &\le \begin{bmatrix} x_i \\ \zeta_i \end{bmatrix}^{\mathsf{T}} \mathbf{W}_i \begin{bmatrix} x_i \\ \zeta_i \end{bmatrix} - \alpha V_1(x_i) + \varepsilon\delta \\ &\le -\alpha V_1(x_i) + \varepsilon\delta.\end{aligned} \tag{43}$$

Applying Schur's complement to $\boldsymbol{W}_i$, the next matrix inequality is obtained:

$$\mathbf{P}\mathbf{A} + \mathbf{A}^{\mathsf{T}}\mathbf{P} - \mathbf{P}B_i K_i - K_i^{\mathsf{T}}B_i^{\mathsf{T}}\mathbf{P} + \alpha\mathbf{P} - \frac{1}{\varepsilon}\mathbf{P}^2 < 0. \tag{44}$$

A necessary condition for Eqn. (44) to be satisfied is that the pair $(\boldsymbol{A}, B)$ be controllable. This means that there exist a set of solutions $(\boldsymbol{P}, K_i, \alpha, \varepsilon)$ that guarantee the negativity of matrix inequality $\boldsymbol{W}_i$ and (43) is fulfilled. Next, by applying the comparison lemma,

$$\frac{dV_1}{dt} = -\alpha\left(V_1 - \frac{\varepsilon\delta}{\alpha}\right), \tag{45}$$

the solution is given by

$$V_1(t) = \left(V_1(t_0) - \frac{\varepsilon\delta}{\alpha}\right)\exp\{-\alpha(t - t_0)\} + \frac{\varepsilon\delta}{\alpha}. \tag{46}$$

Using the Rayleigh–Ritz quotient, the previous equation leads to

$$\begin{aligned}\|x_i\|^2 \le \frac{1}{\lambda_{\min}(\mathbf{P})}\Big\{ & \left(V_1(t_0) - \frac{\varepsilon\delta}{\alpha}\right) \\ & \times \exp\{-\alpha(t_n)\} + \frac{\varepsilon\delta}{\alpha}\Big\},\end{aligned} \tag{47}$$

where $t_n = t - t_0$. Then, for a sufficiently small ε, the energy function satisfies

$$\lim_{t\to\infty}\|x_i\|^2 \le \frac{\varepsilon\delta}{\lambda_{\min}(\mathbf{P})\alpha}. \tag{48}$$

Therefore, for x_i, uniformly ultimately bounded stability is guaranteed. Thus, from (49), we have

$$\left(V_1(t_0) - \frac{\varepsilon\delta}{\alpha}\right)e^{-\alpha(t-t_0)} + \frac{\varepsilon\delta}{\alpha} + \gamma \le \frac{\varepsilon\delta}{\lambda_{\min}(\mathbf{P})\alpha}, \tag{49}$$

and the time T at which the previous inequality is fulfilled is defined by (36).

This is because there is a $V_1(x_i) > 0$ such that $\dot{V}_1(x_i) \le \delta$, where $x_i \in B_b$ and b form (36) as the last bound. From (49), it can be seen that, for control law design, α determines the speed of convergence, whereas ε defines the size of the attraction region. ■

The control inputs for orientations ψ, θ, and ϕ, as well as the height (p_z), are defined as follows:

$$\begin{aligned}\dot{u}_{zz} = &-B_{z2}^{-1}\{\mathbf{k}_{z1}\left(\mathbf{A}_{11}x_{z1}+\mathbf{A}_{12}x_{z2}\right)\\ &+\mathbf{k}_{z2}\left(\mathbf{A}_{21}x_{z1}+\mathbf{A}_{22}x_{z2}+B_{z2}u_{zz}\right)\\ &+\rho_z\text{sign}(\sigma_z(t))\},\end{aligned} \tag{50}$$

$$\begin{aligned}\dot{u}_{\theta} = &-B_{\theta2}^{-1}\{\mathbf{k}_{\theta1}\left(\mathbf{A}_{11}x_{\theta1}+\mathbf{A}_{12}x_{\theta2}\right)\\ &+\mathbf{k}_{\theta2}\left(\mathbf{A}_{21}x_{\theta1}+\mathbf{A}_{22}x_{\theta2}+B_{\theta2}u_{\theta}\right)\\ &+\rho_\theta\text{sign}(\sigma_\theta(t))\},\end{aligned} \tag{51}$$

$$\begin{aligned}\dot{u}_{\phi} = &-B_{\phi2}^{-1}\{\mathbf{k}_{\phi1}\left(\mathbf{A}_{11}x_{\phi1}+\mathbf{A}_{12}x_{\phi2}\right)\\ &+\mathbf{k}_{\phi2}\left(\mathbf{A}_{21}x_{\phi1}+\mathbf{A}_{22}x_{\phi2}+B_{\phi2}u_{\phi}\right)\\ &+\rho_\phi\text{sign}(\sigma_\phi(t))\},\end{aligned} \tag{52}$$

$$\begin{aligned}\dot{u}_{\psi} = &-B_{\psi2}^{-1}\{\mathbf{k}_{\psi1}\left(\mathbf{A}_{11}x_{\psi1}+\mathbf{A}_{12}x_{\psi2}\right)\\ &+\mathbf{k}_{\psi2}\left(\mathbf{A}_{21}x_{\psi1}+\mathbf{A}_{22}x_{\psi2}+B_{\psi2}u_{\psi}\right)\\ &+\rho_\psi\text{sign}(\sigma_\psi(t))\}.\end{aligned} \tag{53}$$

The control strategy developed in the previous section is used similarly for the translational movements p_x and p_y.

3.2. Integral sliding mode control. The mathematical representation of the system used for the design of the ISMC was shown in Eqn. (21). The integral sliding mode strategy design involves two control actions. In general, the control input is defined as (Ullah *et al*., 2020)

$$u_h = u_{h1} + u_{h2}, \tag{54}$$

where u_{h1} is used to stabilize the nominal system in the form of (21) or in dynamic blocks as in (24), u_{h2} is designed to attenuate the effects of the disturbance, and h represents the dynamics of z, ϕ, θ and ψ.

Proposition 3. *Consider a sliding manifold*

$$s_i = G_i\left(x_i - x_{i0} - \int_{t_0}^{t}(\boldsymbol{A}x_i + B_iu_{h1})d\tau\right), \tag{55}$$

where $G_i \in \mathbb{R}^{2\times1}$ is a weight gain. If the control law u_{h2} is given by

$$\begin{aligned}u_{h2} &= -\mathcal{B}_i^{\intercal}G_i^{\intercal}\rho_i\,\text{sign}(s_i),\\ \rho_i &= (G_iG_i^{\intercal})^{-1}R_i, \quad 0 < R_i \in \mathbb{R}^{2\times1},\end{aligned} \tag{56}$$

where $\mathcal{B}_i = TB_i$, $T = [\mathcal{N}_{Bi}, Bi]^{\intercal}$ and $\mathcal{N}_B$ is the null space of B_i, subsequently, after time $t \le t_r$, the dynamic system (21) *is free of the ζ_i effects.*

The sliding surface is related to the solution that guarantees convergence to zero and uses the entire vehicle dynamics. Additionally, G_i is a parameter that aids in vehicle convergence.

Proof. Define a storage function as $V(s_i) = s_i^{\intercal}s_i$. Its dynamic under the control law (56) is given by

$$\dot{V}(s_i) = -s_i^{\intercal}R_i\,\text{sign}(s_i) + s_i^{\intercal}G_i\zeta_i, \tag{57}$$

which means that

$$\dot{V}(s_i) \le \delta_i|s_i| - s_i^{\intercal}R_i\,\text{sign}(s_i) \le -\alpha\sqrt{2}V_i^{1/2}(s_i), \tag{58}$$

where $\alpha = tr(R_i) - \delta_i$. This implies that, at time $t \ge t_{ri}$, the sliding surface converges to zero. ■

Therefore,

$$x_i = x_{i0} + \int_{t_0}^{t}\left(\mathbf{A}x_i + B_iu_{h1}\right)d\tau, \tag{59}$$

and the time variations of the previous relation satisfy the dynamic system

$$\dot{x}_i = \mathbf{A}x_i + B_iu_{h1}, \tag{60}$$

where the input control aim is designed to stabilize this nominal system.

Note that the stabilizing control law u_{zz1} can be designed as a standard conventional linear controller as follows:

$$u_{h1} = -k_ix_i, \;\; k_i \in \mathbb{R}^{1\times2}, \tag{61}$$

where $k_i = [k_{i1}, k_{i2}]^{\intercal}$ and $k_{i1}, k_{i2} \in \mathbb{R}$ are control gains. The procedure for obtaining the control gain k_i is similar to that described in Proposition 2. In the case of the dynamic nominal system described by (60), we have $\zeta_i = 0$, indicating that the bound is $\delta = 0$. Thus, according to (49), the trajectories reach a trivial solution in exponential form with a convergence speed determined by α. The nominal control gains are determined using the optimization process discussed in the previous section. The use of LMI gains improves the performance of nominal control. Furthermore, in the context of ISMCs, the control inputs for the orientation dynamics and height p_z are defined as follows:

$$\begin{aligned}
u_{zz1} &= -k_zx_z, & k_z &= [k_{z1}, k_{z2}]^{\intercal},\\
u_{\theta1} &= -k_\theta x_\theta, & k_\theta &= [k_{\theta1}, k_{\theta2}]^{\intercal},\\
u_{\phi1} &= -k_\phi x_\phi, & k_\phi &= [k_{\phi1}, k_{\phi2}]^{\intercal},\\
u_{\psi1} &= -k_\psi x_\psi, & k_\psi &= [k_{\psi1}, k_{\psi2}]^{\intercal},\\
u_{zz2} &= -\mathcal{B}_z^{\intercal}G_z^{\intercal}\rho_z\,\text{sign}(s_z), & \rho_Z &= (G_zG_z^{\intercal})^{-1}R_z,\\
u_{\theta2} &= -\mathcal{B}_\theta^{\intercal}G_\theta^{\intercal}\rho_\theta\,\text{sign}(s_\theta), & \rho_\theta &= (G_\theta G_\theta^{\intercal})^{-1}R_\theta,\\
u_{\phi2} &= -\mathcal{B}_\phi^{\intercal}G_\phi^{\intercal}\rho_\phi\,\text{sign}(s_\phi), & \rho_\phi &= (G_\phi G_\phi^{\intercal})^{-1}R_\phi,\\
u_{\psi2} &= -\mathcal{B}_\psi^{\intercal}G_\psi^{\intercal}\rho_\psi\,\text{sign}(s_\psi), & \rho_\psi &= (G_\psi G_\psi^{\intercal})^{-1}R_\psi.
\end{aligned} \tag{62}$$

3.3. Adaptive sliding mode controller (ASMC). A widely used controller for stabilizing system dynamics

is the ASMC. While its structure resembles that of the ISMC, it differs in the definition of u_{h1} and the design of u_{h2}. In this study, we employ an ASMC with a sliding surface defined as in the work of Seung-Hun *et al*. (2021):

$$\mathbf{s}_h = \dot{\mathbf{e}}_h + \lambda \mathbf{e}_h, \tag{63}$$

where $e_h = x_h - r_h$ and $\lambda \in \mathbb{R}^{n\times n}$ are positive definite matrices. Adaptive sliding mode control u_h uses the same structure as defined in (54), and u_{h1} is designed as

$$u_{h1} = -k s_h, \tag{64}$$

while the control that mitigates disturbances is defined as

$$u_{h2} = -B^{-1}\hat{\nu}_h \ \mathrm{sign}(s_h), \tag{65}$$

with the dynamics of the adaptive term defined as

$$\dot{\hat{\nu}}_h = \begin{cases} \kappa_{1h}\,(\omega)^{\gamma(t)}\,\gamma(t), & \text{if } 0 < \hat{\nu}_h,\ \min_h |s_h| \geq \varepsilon_2, \\ \kappa_{1h}\kappa_{2h}|s_h|^{-1}, & \text{if } \hat{\nu}_h = 0,\ \min_h |s_h| \geq \varepsilon_2, \\ 0, & \text{otherwise,} \end{cases} \tag{66}$$

where $\omega = \kappa_{2h}^{-1}|s_h|$, $\gamma(t) = \mathrm{sign}(|s_h| - \varepsilon_1)$, ε_1 is a predefined error boundary and $\varepsilon_2 = \varepsilon_1/10 \geq 0$

3.4. $\mathbf{H_\infty}$ controller. An alternative method for stabilizing system dynamics is through optimal control, specifically, H_∞ control. Its goal is to design a stabilizing controller that minimizes the H_∞ norm of the system's transfer function. Put differently, H_∞ control is a robust control design strategy that limits the maximum energy amplification (the H_∞ norm) from disturbances and reference inputs to the resulting errors and control actions, thereby ensuring reliable performance even under worst-case conditions.

The employed H_∞ controller is defined by Razmavar *et al*. (2021) as

$$u_h = -g^T(x)\left(\frac{\partial V}{\partial x}\right)^T = bY - a\eta, \tag{67}$$

where a, b are constants and Y is given as

$$Y = \begin{bmatrix} \sin\psi\ \sin\theta\ \cos\phi - \sin\phi(\cos\psi + \cos\theta) \\ -\sin\theta(1 + \cos\psi\cos\phi) - \sin\psi\sin\phi \\ \cos\psi\ \sin\theta\ \sin\phi - \sin\psi(\cos\phi + \cos\theta) \end{bmatrix}. \tag{68}$$

4. Numerical simulation results

This section presents simulation results obtained in MATLAB Simulink for the control algorithms depicted in Fig. 2, evaluated under two different scenarios. First, the performance of the DSMC, the ISMC, and a PD controller (tuned using an LMI-based algorithm) is compared in terms of disturbance rejection capabilities, with particular emphasis on wind effects during trajectory tracking. Subsequently, the proposed approach is assessed against two widely adopted robust control strategies from the literature, an adaptive sliding mode controller and an H_∞ one, in order to highlight the advantages of the proposed strategy. In both scenarios, the Runge–Kutta method is used with a fixed step of $h = 0.001$ s and a simulation time of 500 s.

Table 1. Parameters of the UAV used for simulation.

Parameter	Value
M	1.6 $\mathrm{K_g}$
J_ϕ, J_θ, J_ψ	1.2 $\mathrm{Nm/rad^2}$
g	9.8 $\mathrm{m/s^2}$

Table 2. Values of each gain used for simulation.

Gain	Value	Gain	Value
k_{z1}	11.0762	$\rho_\phi, \rho_\theta, \rho_\psi$	40
k_{z2}	7.9104	ρ_z	30
k_{x1}	2	R_θ	1
k_{x2}	2.4	G_θ	[0.1, 0.1]
$k_{\theta 1}$	11.0762	R_ϕ	1
$k_{\theta 2}$	7.9104	G_ϕ	[0.1, 0.1]
k_{y1}	2	R_ψ	2
k_{y2}	5	G_ψ	[0.1, 0.1]
$k_{\phi 1}$	11.0762	R_z	2
$k_{\phi 2}$	7.9104	G_z	[0.1, 0.1]
$k_{\psi 1}$	11.0762	$k_{\psi 2}$	7.9104

4.1. Comparison with classic controllers. This simulation aims to compare the performance of the DSMC, the ISMC, and the PD controller (tuned by an algorithm based on the solution of LMIs) by analyzing their ability to reject disturbances such as wind during trajectory tracking. Still, the LMI method does not include translational control. To do this, errors were assessed using performance indices. Similarly, the algorithm for the convex optimization problem based on LMIs was implemented using the CVX Toolbox in MATLAB, and the process to obtain gains was performed offline. This indicates that the gains were generated before the trajectory tracking tests. The parameters of the quadrotor UAV depicted in Fig. 1 are listed in Table 1.

The initial conditions for the positions $(p_x,\ p_y)$ were defined as 2 m and 3 m, respectively, while the initial value of p_z and the initial conditions for the orientations $(\theta,\ \phi,\ \psi)$ were set to zero. The simulation consists of trajectory tracking of the vehicle's translational positions

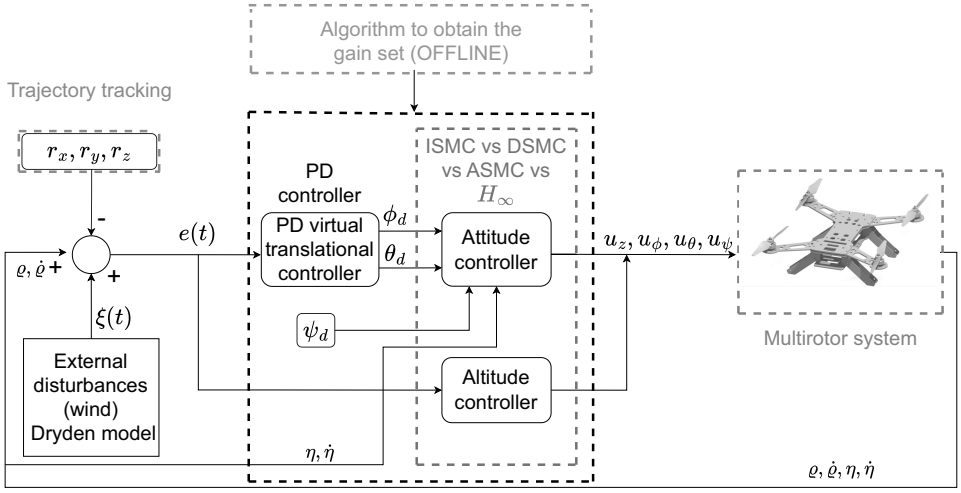

Fig. 2. Block diagram illustrating the simulation process.

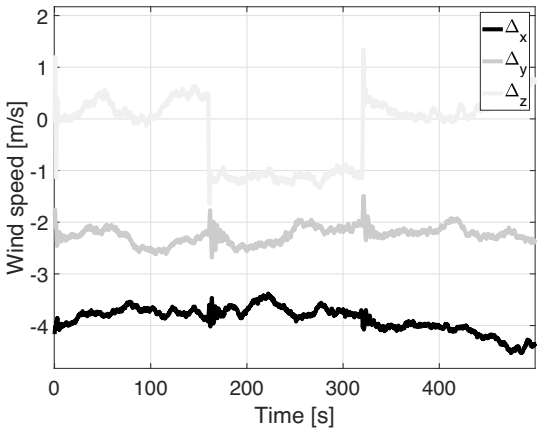

Fig. 3. External disturbances applied to the UAV dynamics.

$(p_x,\ p_y,\ p_z)$ given by

$$\begin{aligned} r_x &= 5\cos(0.15t), \\ r_y &= 5\sin(0.15t), \\ r_z &= 4/(1+e^{-0.9(t-5)}). \end{aligned} \tag{69}$$

Table 2 presents the control gains used for each control strategy implemented in the UAV. The terms ρ_θ, ρ_ϕ, ρ_ψ, ρ_z, and G_θ, G_ϕ, G_ψ, G_z correspond to the DSMC and ISMC.

These values were obtained heuristically to achieve the desired vehicle performance with each implemented strategy. Conversely, gains from $k_{i1} - k_{i2}$ were obtained by solving the optimization problem of the linear matrix inequality described in Proposition 2.

The MATLAB CVX Toolbox was used to generate these gains by setting $\alpha = 0.89$ and $\varepsilon = 0.05$. These values were chosen after performing numerous tests.

The Dryden wind turbulence model was employed as an external disturbance to compare the robustness of the proposed control laws. This model simulates the effects of turbulent air currents, leading to unpredictable variations in the vehicle's positions and orientations. Wind gusts are modeled using the Dryden turbulence model given by Yeager (1998), considering parameters for low altitude and light turbulence given as $L_u = L_v = 200$ m, $L_w = 50$ m, $\sigma_u = \sigma_v = 1.06$ m/s, $\sigma_w = 0.7$ m/s and an altitude of $= 4$ m, where σ_u, σ_v, and σ_w are the intensities of the turbulence along the vehicle frame axes, while L_u, L_v and L_w are spatial wavelengths.

Figure 3 illustrates the disturbance signals used in the simulation tests. The Δ_y line represents the disturbance on p_x, while the Δ_x and Δ_z lines represent the disturbances on p_y and p_z, respectively.

Figure 4 shows the translational error signals for p_x, p_y, and p_z. It should be noted that the ISMC strategy resulted in significantly lower errors than the PD one.

This is more noticeable in the graph for p_z, because when the disturbance occurs the error for the DSMC and ISMC practically stays at zero, whereas in PD the value remains constantly changing. The behavior of the responses obtained for each control strategy between 160 and 200 s is emphasized. This interval corresponds to the time when external disturbances are introduced into the UAV dynamics.

Figure 5 presents the attitude performance of the vehicle. It shows a close-up in the interval from 160 s to 170 s to highlight the performance of the controllers when external disturbances are introduced.

Figure 6 illustrates each controller's performance when the vehicle tracks the same path. Also, it shows that the PD controller exhibits more oscillations the moment

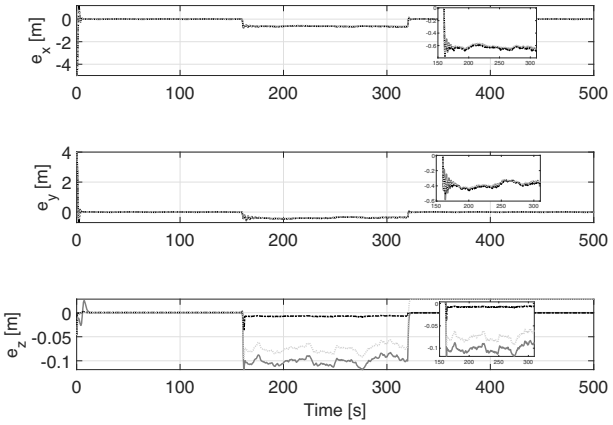

Fig. 4. Translational error signals. Solid line: PD controller error signal, dash-dotted line: DSMC error signal, dotted line: ISMC error signal.

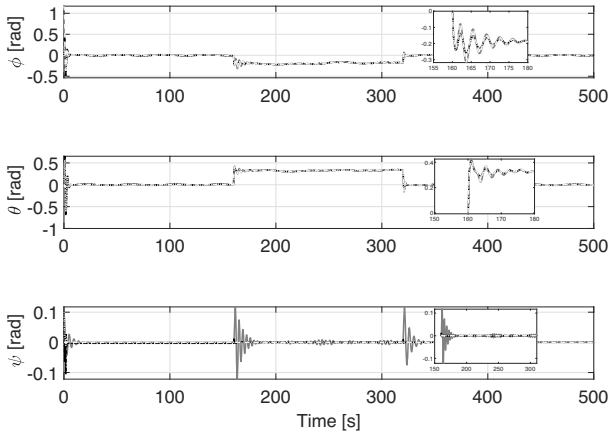

Fig. 5. UAV attitude during the flight mission. Dashed line represents the desired position, solid line: angular position signals obtained from the PD controller, dash-dotted line: DSMC, dotted line: one obtained with the ISMC.

the disturbance is introduced.

The performance indices IAE, ISE, ITAE, and ITSE were used to assess the effectiveness of control strategies and establish a clear comparison. The indices are defined as follows:

$$\text{IAE} = \int_0^t \|\mathbf{e}(\tau)\|\, d\tau, \qquad \text{ISE} = \int_0^t \|\mathbf{e}(\tau)\|^2\, d\tau,$$
$$\text{ITAE} = \int_0^t \tau\|\mathbf{e}(\tau)\|\, d\tau, \qquad \text{ITSE} = \int_0^t \tau\|\mathbf{e}(\tau)\|^2\, d\tau, \tag{70}$$

where $\|\mathbf{e}\| = (\mathbf{e}^\intercal\mathbf{e})^{\frac{1}{2}}$ and $\|\mathbf{e}\|^2 = \mathbf{e}^\intercal\mathbf{e}$. The ISE index analyzes the difference between the underdamped and overdamped responses of the vehicle. The ITSE index provides the same information as ISE but penalizes the vehicle's performance based on the time elapsed between the start of the flight and its actual position. The IAE index provides information on transient responses and assesses performance adequacy, while ITAE offers similar information but penalizes performance over time.

Table 3 displays the results of the error index (UAV orientation) described earlier for the flight mission performed by the multirotor vehicle. For example, the table shows that the ISMC reduced the error by 36.88% compared to the PD strategy for the IAE criterion. The ISE criterion indicated that the ISMC reduced the error by 20.31% compared to the DSMC. Furthermore, the ITAE and ITSE criteria showed that the ISMC outperformed the DSMC and the PD controller in terms of error.

Furthermore, Table 4 shows the analysis of IAE, ISE, ITAE, and ITSE for the position p_z. The results demonstrate the effectiveness of the proposed control algorithms. The ISE analysis showed that the ISMC outperformed the PD controller by 44.06% in terms of performance, particularly in relation to transient

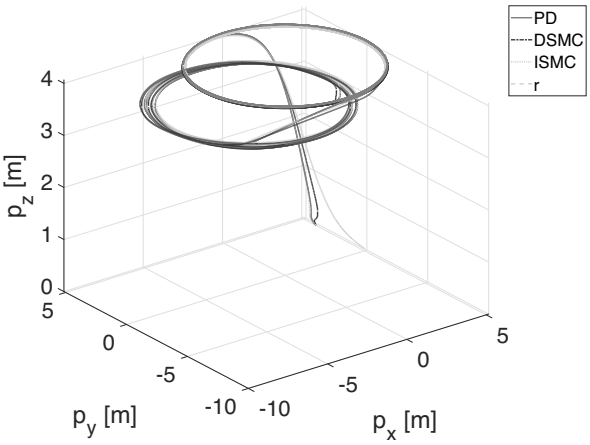

Fig. 6. UAV 3D view of all paths of the vehicle with the ISMC, DSMC and the PD controller.

Table 3. Error indices of the UAV orientation.

Controller	IAE	ISE	ITAE	ITSE
PD	2.562	0.079	526.8	2.856
DSMC	2.533	0.064	569.7	4.842
ISMC	**1.617**	**0.051**	**345.6**	**0.997**

responses. Furthermore, the values obtained for the ITAE index exhibited a reduction of 24.36% compared to IAE, indicating that, as time passed, the ISMC showed better performance. However, based on these altitude results, the DSMC strategy outperforms the PD and ISMC approaches.

Additionally, the obtained values for the ITSE index exhibited a 28.27% reduction compared to the PD controller, indicating that, as time progressed, the ISMC showed better performance compared to the PD controller. Based on the errors indices of the UAV orientation,

Table 4. Error indices of the UAV altitude.

Controller	IAE	ISE	ITAE	ITSE
PD	10.32	0.652	2426	154.2
DSMC	**0.8344**	**0.0039**	**186.4**	**0.8275**
ISMC	10.93	0.3647	3463	110.6

Table 5. Errors indices of the UAV translation.

Controller	IAE	ISE	ITAE	ITSE
ASMC	834.5	3414	2×10^5	8.16×10^5
H_∞	817.9	3407	1.95×10^5	8.12×10^5
ISMC	**796.7**	**3289**	$\mathbf{1.89 \times 10^5}$	$\mathbf{7.83 \times 10^5}$

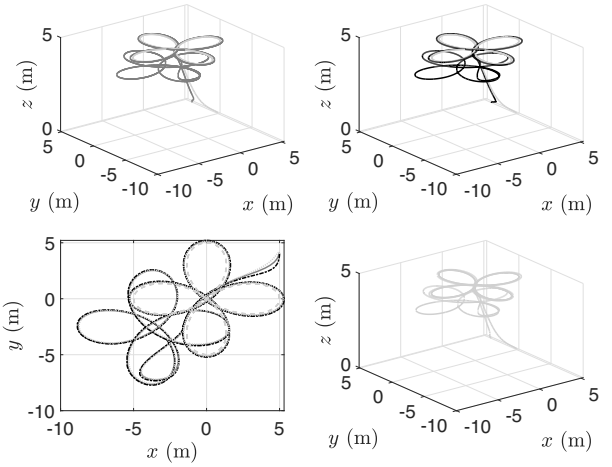

Fig. 7. 3D trajectory of the UAV under H_∞, the ASMC, and the ISMC. Solid line: H_∞ controller, dash-dotted line: ASMC, dotted line: ISMC, dashed line: desired trajectory.

the ISMC strategy outperforms the PD and DSMC approaches. In Table 3, the error vector $\mathbf{e}$ includes errors associated with ϕ, θ, and ψ. In contrast, Table 4 describes the error indices concerning only altitude dynamics.

To analyze the energy consumption of the resulting control laws, the following energy equation is used:

$$E_u = \int_0^t u(\tau)^\intercal u(\tau) d\tau. \tag{71}$$

The results show that the energy consumed during the flight mission by the PD control was $E_{u_{PD}} = 1.322 \times 10^5$ N^{2}m^{2}s, for the DSMC it was $E_{u_{DSMC}} = 1.253 \times 10^5$ N^{2}m^{2}s, and for the integral sliding mode control it was $E_{u_{ISMC}} = 1.570 \times 10^5$ N^{2}m^{2}s. The PD controller reduced the required energy consumption by 15.8% compared to the ISMC, while the DSMC consumed 20.2% less energy. Based on these data, it is clear that the DSMC outperformed the ISMC and PD control strategies in terms of energy consumption.

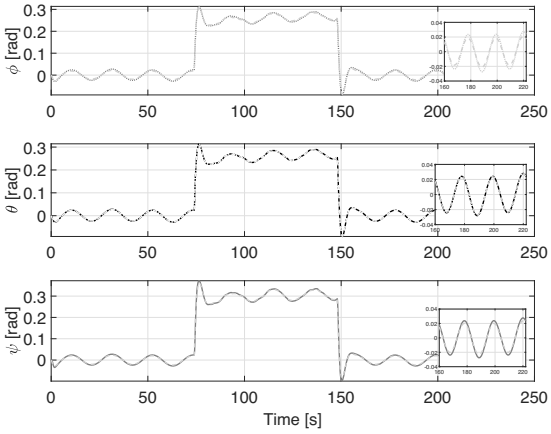

Fig. 8. UAV attitude during the flight mission. Dashed line: desired position, black line: H_∞ controller, dash-dotted line: ASMC, dotted line: ISMC.

4.2. Comparison with robust controllers. An analysis of the ISMC, the ASMC, and the H_∞ controller is presented. Figure 7 shows the translational tracking errors obtained with each controller when applied to a four-leaf rose trajectory. It should be noted that the ISMC strategy is the controller with the lowest steady-state error compared to the other two. The H_∞ controller and the ASMC show similar performance with or without disturbance. In contrast, Fig. 8 shows that the ASMC exhibits the best behavior when the controller follows the desired attitude trajectory, and Table 5 reinforces this observation.

The energy consumed by each controller to perform the rose trajectory was $E_{uISMC} = 1.614 \times 10^5$ N^{2}m^2 s, $E_{uH_\infty} = 1.342 \times 10^5$ N^{2}m^{2}s and $E_{uASMC} = 1.343 \times 10^5$N^2 m^{2}s. The ASMC saves 16.79% energy compared to the ISMC, and H_∞ saves 0.074% compared to the ASMC. The data indicate that the ISMC has the best performance in the translation dynamics, but the best behavior in attitude dynamics is obtained with the ASMC.

5. Conclusions

This study presented an LMI-based algorithm for offline tuning of dynamic and integral sliding-mode controllers (DSMC and ISMC) for quadrotor trajectory tracking. The approach ensured finite-time convergence of the sliding surfaces, yielding PD-like structures while guaranteeing ultimate uniform stability under uncertain dynamics and Dryden-modeled wind disturbances. Simulation results showed that the DSMC reduced altitude errors by 94.61% compared to the alternative controllers, while the PD controller achieved superior transient response with a 29.94% error reduction. For rotational dynamics, the ISMC demonstrated strong disturbance rejection (79.40% performance index) but introduced significant chattering,

whereas the DSMC provided smoother responses with lower energy demand. Thus, the ISMC offered higher disturbance attenuation, while the DSMC proved more effective for practical implementation due to reduced chattering. Overall, the proposed LMI-based tuning strategy simplified controller design and facilitated systematic comparison, enabling the selection of the most suitable control scheme according to system performance requirements. The second comparative analysis demonstrates the advantage of using the ISMC in quadcopters with the use of a rose trajectory. In translational dynamics, the ISMC demonstrates around 4.52% better performance in contrast to the other two controllers, which is supported by the error indices. But, the ASMC denotes the best trajectory tracking compared with H_∞ and the ISMC. Finally, the H_∞ controller consumed less energy.

Future work will involve performing model-, software-, and hardware-in-the-loop simulations to assess the proposed strategies in a controlled environment, followed by validation of their feasibility using a physical prototype.

References

Ahmad, S., Abid, M. and Hussain, S. (2022). Adaptive sliding mode-based active disturbance rejection control for a quadcopter, *Transactions of the Institute of Measurement and Control* **44**(16): 3176–3190.

Da Silva, G. and Moreira, W. (2022). Sliding mode control with Gaussian process regression for underactuated mechanical systems, *IEEE Latin America Transactions* **20**(6): 963—969.

Din, S., Khan, Q., Tu, Z., Rehman, F. and Akmeliawanti, R. (2018). A comparative experimental study of robust sliding mode control strategies for underactuated systems, *IEEE Access* **6**: 1927–1939.

Eker, I. (2006). Sliding mode control with PID sliding surface and experimental application to an electromechanical plant, *ISA Transactions* **45**(1): 109–118.

Eltayeb, A., Rahmat, M., Basri, M., Eltoum, M. and ElFerik, S. (2020). An improved design of an adaptive sliding mode controller for chattering attenuation and trajectory tracking of the quadcopter UAV, *IEEE Access* **8**: 205968–205979.

Falcón, R., Ríos, H. and Dzul, A. (2019). Comparative analysis of continuous sliding-modes control strategies for quad-rotor robust tracking, *Control Engineering Practice* **90**: 241–256.

García, L., Dzul, A., Lozano, R. and Pegard, C. (2013). *Quad Rotorcraft Control Vision-Based Hovering and Navigation*, Springer, London.

García, O., Ordaz, P., Santos, O., Salazar, S. and Lozano, R. (2019). Backstepping and robust control for a quadrotor in outdoors environments: An experimental approach, *IEEE Access* **7**: 40636–40648.

Herrera, M., Camacho, O., Leiva, H. and Smith, C. (2020). An approach of dynamic sliding mode control for chemical processes, *Journal of Process Control* **85**(1): 112–120.

Khan, A. and Nasreen (2021). A comparative study between two different adaptive sliding mode control techniques, *International Journal of Applied and Computational Mathematics* **7**(150): 1–18.

Lei, S., Yongming, L. and Shaocheng, T. (2024). Integral sliding mode control for uncertain impulsive stochastic systems, *European Journal of Control* **76**: 1–7.

Liu, H., Li, D., Yu, Y. and Zhong, Y. (2014). Robust trajectory tracking control of uncertain quadrotors without linear velocity measurements, *33rd Chinese Control Conference, Nanjing, China*, pp. 4169–4174.

Mofid, O., Mobayen, S. and Wong, W. (2021). Adaptive terminal sliding mode control for attitude and position tracking control of quadrotor UAVs in the existence of external disturbance, *IEEE Access* **9**: 3428–3440.

Ordaz, P., Espinoza, E., Munõz, F., Carrillo, L., Romero, H. and Lozano, R. (2018). Nonlinear control and trajectory tracking of an unmanned aircraft system based on a complete state space representation, *IFAC-PapersOnLine* **51**(13): 561–566.

Ordaz, P., Ordaz, M., Cuvas, C. and Santos, O. (2019). Reduction of matched and unmatched uncertainties for a class of nonlinear perturbed systems via robust control, *International Journal of Robust and Nonlinear Control* **29**(8): 2510–2524.

Poznyak, A., Polyakov, A. and Azhmyakov, V. (2014). *Attractive Ellipsoids in Robust Control*, Vol. 1, Birkhauser, Cham.

Raiesdana, S. (2020). Control of quadrotor trajectory tracking with sliding mode control optimized by neural networks, *Proceedings of the Institution of Mechanical Engineers I: Journal of Systems and Control Engineering* **234**(10): 1101–1119.

Razmavar, V., Ali-Talebi, H. and Abdollahi, F. (2021). A composite controller based on nonlinear h_∞ and nonlinear disturbance observer for attitude stabilization of a flying robot, *Indonesian Journal of Electrical Engineering and Computer Science* **22**(1): 270–276.

Rehman, A., Mazhar, N., Raza, A. and Mumtaz, F. (2021). Sliding mode control of quadrotor UAV using parabolic sliding surface, *2021 International Conference on Innovative Computing (ICIC), Lahore, Pakistan*, pp. 1–6.

Ríos, H., Falcón, R., González, O. and Dzul, A. (2019). Continuous sliding-mode control strategies for quadrotor robust tracking: Real-time application, *IEEE Transactions on Industrial Electronics* **66**(2): 1264–1272.

Roux, T., Fridman, L. and Hsu, L. (2023). *Sliding-Mode Control and Variable-Structure Systems*, Vol. 1, Springer, London.

Seung-Hun, H., Manh-Son, T. and Duc-Thien, T. (2021). Adaptive sliding mode control for a robotic manipulator with unknown friction and unknown control direction, *Applied Science* **11**(11): 3919.

Ullah, S., Mehmood, A. and Khan, Q. (2020). Robust integral sliding mode control design for stability enhancement of under-actuated quadcopter, *International Journal of Control, Automation and Systems* **18**: 1671–1678.

Yeager, J.C. (1998). Implementation and testing of turbulence models for the F18-HARV simulation, *Technical report*, Lockheed Martin Engineering & Sciences, Hampton, https://ntrs.nasa.gov/citations/19980028448.

Yongwei, Z. and Shunchao, Z. (2024). Integral sliding mode-based event-triggered optimal fault tolerant tracking control of continuous-time nonlinear systems, *European Journal of Control* **79**: 101021.

Daniel Benítez Morales holds a bachelor's degree in mechatronics from the Polytechnic University of Pachuca and an MSc degree in automatization and control from the Autonomous University of Hidalgo State, Hidalgo, Mexico. Currently, he is studying for a PhD. His research interests include UAVs and UGV applications, self-driving cars, and control of this kind of vehicles.

Jovani Ortega Ventura received his bachelor's degree in electronic and telecommunications engineering and his MSc degree in automatic control from the Autonomous University of Hidalgo State, Hidalgo, Mexico, in 2015 and 2018, respectively. He is currently pursuing his PhD degree. His research interests include nonlinear control of electromechanical systems, sliding mode control, and unmanned aerial vehicles (UAVs).

Jesus P. Ordaz received his bachelor's degree in electronic and telecommunications engineering and his MSc degree in automatic control from the Autonomous University of Hidalgo State (UAEH), Hidalgo, Mexico, in 2004 and 2007, respectively, and his PhD degree in automatic control from CINVESTAV, Mexico, in 2012. He is currently with UAEH. His research interests include robust and adaptive control, system identification, and observation.

Eduardo S. Espinoza received his PhD degree in automatic control from the Center for Research and Advanced Studies of the National Polytechnic Institute, Mexico, in 2013. He was a postdoctoral researcher at the University of Nevada, USA, in 2016. At present, he holds a professorial position at CINVESTAV, Mexico. His research interests include neuromorphic computing, design, and control of eVTOL aircraft.

Received: 15 May 2025
Revised: 2 October 2025
Re-revised: 3 November 2025
Accepted: 21 November 2025